npj | climate and atmospheric science

Article

Published in partnership with CECCR at King Abdulaziz University

https://doi.org/10.1038/s41612-024-00855-3

# Vertical and spatial differences in ozone formation sensitivities under different ozone pollution levels in eastern Chinese cities



Zhuang Wang[1,2], Hao Zhang[1,2], Chune Shi[1,2], Xianguang Ji[3], Yizhi Zhu[4], Congzi Xia[5], Xiaoyun Sun[1,2], Meng Zhang[1,6], Xinfeng Lin[2], Shaowei Yan[2], Yuan Zhou[7,8], Chengzhi Xing[9] ✉, Yujia Chen[1,2] ✉ & Cheng Liu[9,10,11,12] ✉

Ozone is the primary air pollutant in eastern China during the warm season. Clarifying the differences in the spatio–temporal evolution of the ozone formation sensitivity between ozone polluted days and clean air days is key for the precise formulation of ozone prevention policies. By combining ground–and satellite–based remote sensing with ground station observations, we identified large spatio–temporal differences in the ozone formation sensitivity in eastern Chinese cities under different ozone pollution levels. Diurnally, the $NO_2$ concentration was higher in the morning and lower at noon on the ozone exceedance days. The HCHO concentration was higher throughout the day, and the transition limited regime or $NO_x$–limited regime contributed more to the ozone formation sensitivity on the ozone exceedance days. Vertically, the ratio of HCHO to $NO_2$ (FNR) was higher on ozone exceedance days, and the contributions of $NO_x$–limited regime at 0–2 km and the transition limited regime at 0–1 km on ozone exceedance days increased considerably. Spatially, HCHO in the North China Plain and middle–lower Yangtze River Plain was significantly increased on ozone exceedance days, while the $NO_2$ concentration in the southeast hills was increased on ozone exceedance days. The difference in FNR values between northern and southern cities in eastern China on $O_3$ exceedance days narrowed, and the ozone formation sensitivity in eastern China tended to be under a transition limited regime. The shifts in the ozone formation sensitivity under different ozone pollution levels implies that controlling only one of the precursors cannot achieve the best $O_3$ prevention effect, and the most appropriate ratio of $O_3$ precursor emission reductions should be designed according to ozone formation sensitivity in the different regions.

In recent years, with the implementation of a series of emission reduction measures in China, primary air pollutants, notably fine particulate matter ($PM_{2.5}$), nitrogen dioxide ($NO_2$), sulfur dioxide ($SO_2$), and carbon monoxide (CO), have shown significant decreasing trends[1,2]. However, the secondary air pollution represented by ozone ($O_3$) has not been effectively controlled[3–5]. Particularly in summer, $O_3$ has replaced $PM_{2.5}$ as the primary air pollutant in eastern China and may persist in the country for a long time to come. Near–surface $O_3$ is formed from volatile organic compounds (VOCs) and nitrogen oxides ($NO_x$) through a series of complex chemical reactions under sunlight[6,7]. Complex non–linear relationships exist between VOCs, $NO_x$, and $O_3$. In the $NO_x$–limited regime, when the VOC concentration remains constant, decreasing $NO_x$ concentrations result in decreasing $O_3$ concentrations. In the VOC–limited regime, when $NO_x$ remains unchanged, lowering the VOC concentration results in lower $O_3$ concentrations. However, in the VOC–limited regime, if the VOC concentration remains constant, reducing the $NO_x$ concentration may lead to an increase in the $O_3$ concentration[6,8]. Therefore, fully understanding the mechanism of $O_3$ generation and clarifying limiting regimes for $O_3$ formation are the basis for the development of $O_3$ pollution control measures.

A full list of affiliations appears at the end of the paper. ✉e-mail: xingcz@aiofm.ac.cn; chenyj18@mail.ustc.edu.cn; chliu81@ustc.edu.cn

Empirical kinetics modeling approach (EKMA) curves based on offline sampling data at ground stations are the main method currently used to investigate $O_3$ formation sensitivity (OFS)[9,10]. However, owing to the wide variety of VOCs and their different activities, the heavy workload of offline analysis and long analysis cycles affect the timeliness of $O_3$ pollution control. Ambient formaldehyde (HCHO), which is mainly generated by the oxidation of VOCs, has a short atmospheric lifetime and is positively correlated with the peroxyl radical ($RO_2$). With limited information, HCHO can be used to represent the total reactivity of VOCs to analyze the OFS[11,12]. In addition, because of the short lifetime of $NO_x$, $NO_2$ is usually considered as a substitute for $NO_x$ concentration[13]. Based on these assumptions, many studies have used the ratio of HCHO (a proxy for VOCs) to $NO_2$ (a proxy for $NO_x$) (FNR) to characterize the OFS[14–17], namely, FNR = HCHO/$NO_2$. In particular, satellite observations can simultaneously identify these two compounds, which has prompted researchers to study the spatial heterogeneity of the $O_3$ formation mechanism through FNR. For example, Ren et al.[14] found that the VOC–limited regime was widespread in Chinese mega–city clusters, such as the North China Plain (NCP), Yangtze River Delta (YRD), and Pearl River Delta (PRD), whereas the $NO_x$–limited regime dominated most of the remaining areas. However, satellite observations provide only one FNR observation per day, which may not be fully representative of the daytime OFS. In addition, satellite measurements can only provide tropospheric column concentrations and cannot identify the OFS at different heights. Therefore, high temporal resolution HCHO and $NO_2$ data are required to explore the daily evolution of the OFS. Moreover, temporal and regional differences will lead to different spatio–temporal characteristics of $O_3$ precursors ($NO_x$ and VOCs) in different regions. Therefore, a comprehensive understanding of the spatial and temporal characteristics of $O_3$ and its precursors is essential for regional control of atmospheric photochemical pollution.

Multi–axis differential optical absorption spectroscopy (MAX–DOAS) enables long–term rapid simultaneous vertical profile measurements of atmospheric trace gases; therefore, it is widely used in the diagnosis of atmospheric OFS. For example, Hong et al.[18] and Lin et al.[19] employed MAX–DOAS observations in Guangzhou to determine that diurnally, the near surface was basically in the VOC–limited regime in the morning, and in a transition limited regime in the noon and afternoon. Vertically, the OFS varied with height, from a VOC–limited regime (0.02–0.22 km) to a transition limited regime (0.22–0.42 km) and an $NO_x$–limited regime (0.42–2.02 km). Hu et al.[20] observed $O_3$ and its precursor profiles ($O_3$, HCHO, $NO_2$) using MAX–DOAS in the NCP, YRD, and PRD simultaneously and found that the VOC–limited regime dominated near the surface, while the contribution of the $NO_x$–limited regime increased with increasing altitude. Peng et al.[21] combined the Geostationary Environmental Monitoring Spectrometer (GEMS) with MAX–DOAS measurements to analyze the OFS in the NCP region and noted that factors such as spatio–temporal characteristics and seasonality must be considered when formulating $O_3$ control policies. Therefore, satellites combined with ground–based MAX–DOAS observations can provide a feasible method for investigating the spatio–temporal distribution of key $O_3$ precursors and determining the OFS in the lower troposphere.

Previous studies based on satellites and MAX–DOAS have mainly focused on the spatio–temporal characteristics of the OFS over the entire observation period or $O_3$ pollution period. The differences in meteorological conditions between $O_3$ pollution days and clean days have been revealed by a large number of studies[3,5,22]. However, the differences in the spatio–temporal evolution characteristics of $O_3$ precursors and the OFS between $O_3$ pollution days and clean days have received less research attention[18]. Clarifying these differences is the key to accurately preventing and controlling $O_3$ pollution and reducing the number of $O_3$ exceedance days, because it is difficult to accurately understand the detailed driving force of ozone pollution by merely investigating the entire observation period or $O_3$ pollution period, especially in the context of the high ozone precursor concentrations in eastern Chinese cities. In this study, long–term ground–based MAX–DOAS and satellite observations were combined to investigate the vertical structural features and differences, as well as the regional distribution features and differences, in the OFS in eastern Chinese cities under different ambient $O_3$ levels. This study aims to provide a better understanding of the driving force and prevention methods for $O_3$ pollution in eastern Chinese cities from the perspective of its vertical and spatial evolution. Note that all of the times mentioned in this study refer to the local time.

## Results

### Spatial and vertical variations in $O_3$ and its precursors in eastern China

The concentration of industry, dense population, and heavy traffic in eastern China lead to high emissions of $NO_x$ and VOCs, which are the main precursors for $O_3$ formation[2,22]. Influenced by anthropogenic emissions, vegetation activity, and heat source emissions[23–25], the Taihang Mountains form a geographical barrier that prevents the transport of high concentrations of $NO_x$ and VOCs from the south to the north (Fig. 1). Thus, $NO_2$ is mainly concentrated in urban agglomerations (0.6–1.3 $\times 10^{16} molecules/cm^2$) in the NCP (Beijing, Tianjin, Hebei, Shandong, northern Henan, northern Anhui, and northern Jiangsu) and the Middle–Lower Yangtze River plain (MLYRP: Shanghai, southern Jiangsu, and northern Zhejiang). In contrast, the southeastern hilly areas (western Hubei, Hunan, Jiangxi, southern Anhui, and southern Zhejiang), which have high vegetation cover, have relatively low $NO_2$ concentrations (less than $0.6 \times 10^{16} molecules/cm^2$). High HCHO concentrations ($1.1–1.9 \times 10^{16} molecules/cm^2$) are distributed over a much wider area, occupying almost the entirety of eastern China, and the HCHO levels are mainly affected by industrial emissions, biogenic VOC in vegetation, and thermogenic emissions from biomass burning[24,25]. As a result, high HCHO concentrations exceeding $1.5 \times 10^{16} molecules/cm^2$ during April–October 2020–2023 are mainly concentrated on the southern side of the Taihang Mountains, and the HCHO concentrations north of the Taihang Mountains are below $1.1 \times 10^{16} molecules/cm^2$.

High maximum daily 8–h average $O_3$ (MDA8O3) concentrations (>85 ppb) are primarily distributed in the NCP (Fig. 1c), particularly in Hebei, Henan, Shandong, Jiangsu, and northern Anhui, with relatively low $O_3$ concentrations in the southeastern hilly areas. Overall, $O_3$ in eastern China shows an increasing spatial distribution from south to north. Differences in the regional distributions of $O_3$ precursors (HCHO and $NO_2$) inevitably lead to differences in the OFS. FNR derived by Tropospheric Monitoring Instrument (TROPOMI) shows that most cities in the NCP and the MLYRP have FNR values ranging from 1.2–2.6 (mainly in the VOC–limited regime, details refer to METHODS M4), which is considerably lower than that of the southeastern hilly area (>3, mainly in the transition limited regime or $NO_x$–limited regime, details refer to METHODS M4). The spatial distribution of FNR exhibits a diametrically opposite trend to that of the $O_3$ concentration (Supplementary Fig. 1), showing a significant negative correlation, with a Pearson's correlation coefficient of –0.46 ($p < 0.01$). In other words, regions with high $O_3$ concentrations have low FNR values and are more sensitive to VOC concentrations in eastern China.

Figure 2 shows the mean diurnal changes in the vertical distributions of $NO_2$, HCHO, and FNR in Hefei, Huaibei, and Taian. The surface $O_3$ concentrations in Hefei, Huaibei, and Taian increase rapidly from 08:00 to 13:00, with a significant slowdown after 13:00. The diurnal variation of the $NO_2$ vertical distribution shows that $NO_2$ is mainly confined below 0.3 km, with average concentrations of approximately 5.2 ppb in Hefei, 4.1 ppb in Huaibei, and 5.0 ppb in Tai'an. This is primarily attributed to ground–based emission sources[26], such as residential areas, industrial facilities, and power plants. It is worth noting that the peak $NO_2$ concentration occurs between 8:00 and 10:00, and the mean concentration exceeds 9.0 ppb in Hefei, 7.7 ppb in Huaibei, and 10.2 ppb in Taian, corresponding to the morning rush hour[27]. The decreased $NO_2$ concentrations at noon and in the afternoon are attributed to the increase in light intensity during the warm season, which accelerates $NO_2$ photolysis. The diurnal variation in the vertical distribution of HCHO is significantly different from that of $NO_2$. It can be clearly seen

that HCHO is mainly distributed below 0.6 km. The average HCHO vertical profiles in Hefei and Huaibei peak at the heights of 0.1–0.3 km (5.3 ppb in Hefei and 4.4 ppb in Huaibei) rather than at the bottom layer. The peak HCHO concentration in Taian after 11:00 also appears at 0.1–0.3 km. The most probable reason for the elevation of the HCHO layer during the period of 10:00–16:00 is that more active photochemical reactions occur in the elevated layer (0.1–0.3 km)[28]. For example, owing to the upward transport of its precursors (such as isoprene) to the elevated layer, it is oxidized to secondary HCHO under sunlight, which is consistent with the results of previous studies on atmospheric pollution in China[29]. Overall, the diurnal variation in HCHO during the warm season in eastern China shows a continuous upward trend in the morning, peaking at around 11:00, and the trend then remains relatively stable until the afternoon. This pattern may be attributed to the intense and persistent sunlight and favorable weather conditions during the warm season in eastern China, where vegetation releases large amounts of biogenic precursors[30], and the intense solar radiation from midday to afternoon enhances the photochemical oxidation process, leading to the accumulation of HCHO near the surface.

The OFS vertical distributions also show significant diurnal variations, influenced by the differences in the diurnal variations of the $NO_2$ and HCHO vertical distributions. Figure 2j–l shows that the diurnal variations in the FNR vertical structures in Hefei, Huaibei, and Taian have almost the same trends. The FNR value below 0.5 km is less than 1.5 at 08:00–10:00, the thresholds for the transition limited regime of Hefei, Huaibei, and Tai'an were 1.94–2.43, 2.01–2.59, and 1.98–2.56, respectively (details refer to METHODS M4). Thus, the OFS is in the VOC–limited regime. With the enhancement of solar radiation, the intense photochemical reaction causes the HCHO concentration to increase, the $NO_2$ concentration to decrease, and the FNR value to increase continuously, and it usually reaches a maximum value at 12:00–14:00 (1.8–2.1, mainly in the transition limited regime). After 14:00, the FNR value continues to decrease, and the OFS shifts to the VOC–limited regime again. In terms of the vertical distribution, the FNR values below 1.5 km continue to increase with height, which is caused by the difference in the vertical distribution of HCHO and $NO_2$; $NO_2$ is more concentrated near the surface, whereas high concentrations of HCHO can extend to higher altitudes. Based on the surface fitted FNR threshold, the OFS vertical distributions in eastern China can be summarised as follows: (1) In the early morning (8:00–10:00), the VOC–limited regime usually occurs below 0.5 km, the transition limited regime usually occurs between 0.5 and 0.7 km, and the $NO_x$–limited regime usually occurs above 0.7 km. (2) At noon (12:00–14:00), a transition limited regime usually occurs below 0.3 km, and a $NO_x$–limited regime usually occurs above 0.3 km.

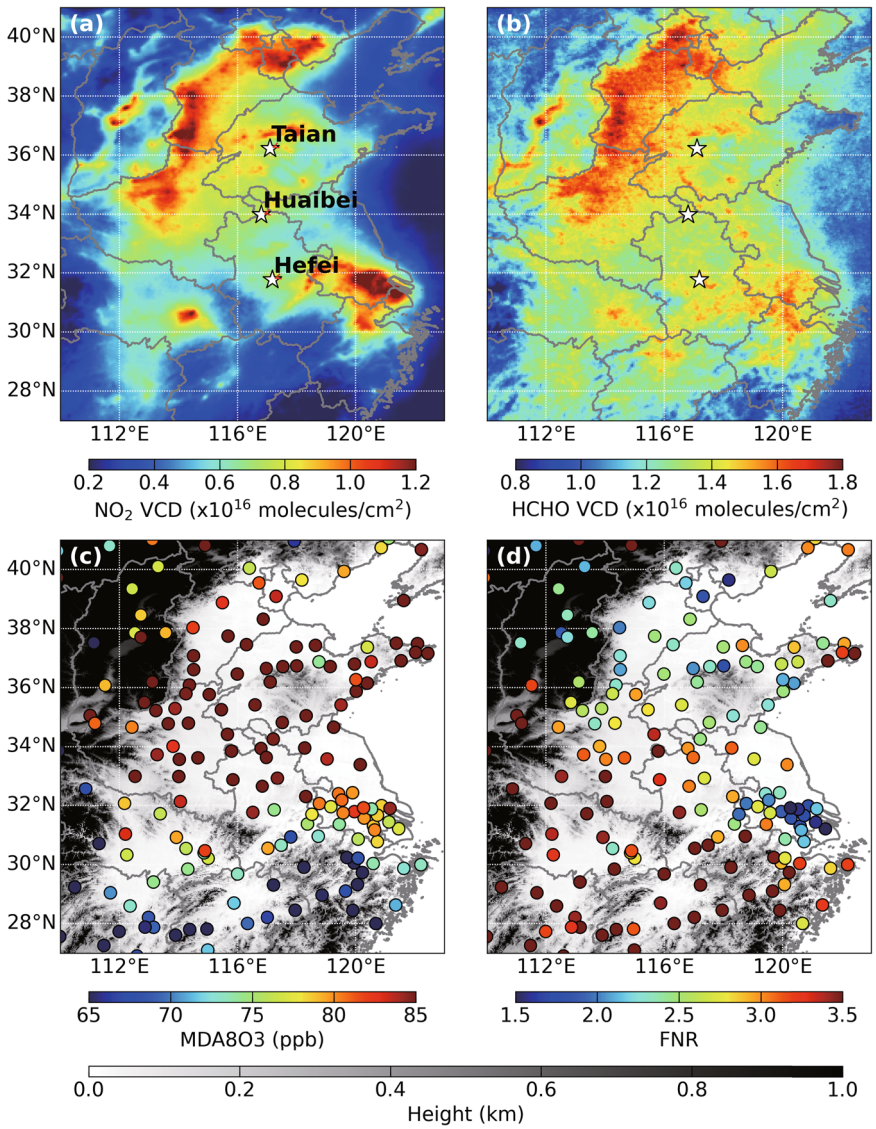


**Fig. 1 | Spatial distribution of ozone and its precursors.** Spatial distributions of tropospheric mean **a** $NO_2$ VCD, **b** HCHO VCD, **c** surface mean MDA8O3, and **d** mean FNR derived from TROPOMI observations in eastern China during April–October, 2020–2023. The white stars in (**a**) represent the cities equipped with ground-based MAX–DOAS observations.

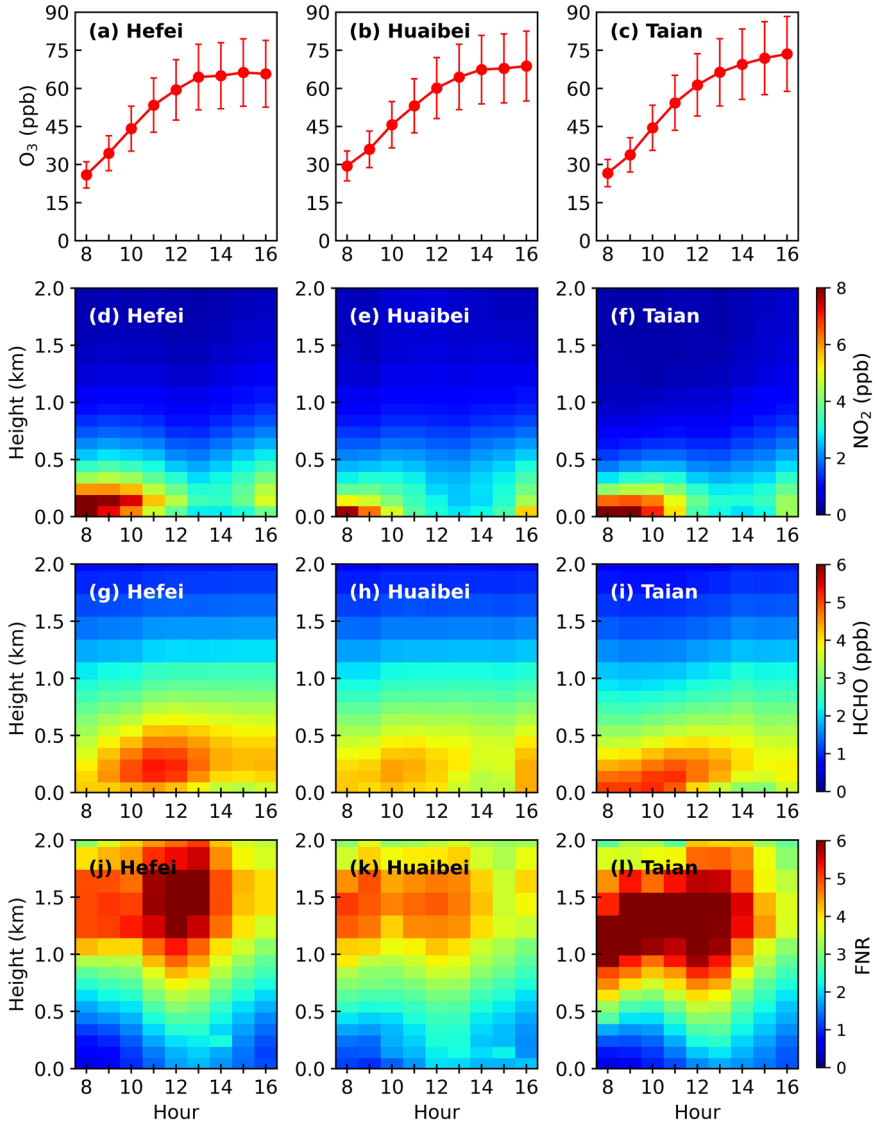


**Fig. 2 | Diurnal variations of $O_3$ and its precursors.** Mean diurnal variations in the surface $O_3$ concentrations in **a** Hefei, **b** Huaibei, and **c** Tai'an during April–October, 2020–2023. Mean diurnal variations in the **d**–**f** $NO_2$ vertical distributions, **g**–**i** HCHO vertical distributions, and **j**–**l** FNR vertical distributions in Hefei, Huaibei, and Tai'an during April–October, 2020–2023.

### Vertical difference of ozone precursors under different ozone pollution levels

Many previous studies have investigated the relationship between $O_3$ and its precursors during $O_3$ exceedance days[10,31–33]. In this study, we focus on investigating the differences in the spatial and temporal evolution of vertical distribution of $O_3$ precursors (HCHO, $NO_2$) under different $O_3$ pollution levels. The entire observation period was classified into $O_3$ level 0 days (clean days, MDA8O3 < 100 μg/m$^3$), $O_3$ level 1 days (light pollution days, 100 μg/m$^3$ < MDA8O3 < 160 μg/m$^3$), and $O_3$ exceedance days (heavy pollution days, MDA8O3 > 160 μg/m$^3$), details refer to METHODS M2. Supplementary Fig. 2 shows the mean diurnal variations in the surface $O_3$ and$\Delta O_3$ concentrations in Hefei, Huaibei, and Tai'an under different $O_3$ pollution levels during April–October 2020–2023;$\Delta O_3$ is defined as the difference in $O_3$ concentration between two adjacent hours. Significant differences are observed in the diurnal variations in surface $O_3$ concentrations in Hefei, Huaibei, and Tai'an under different $O_3$ pollution levels. The cumulative $O_3$ concentration is higher in the early morning on the $O_3$ exceedance days. The mean $O_3$ concentration at 7:00 on $O_3$ level 0 days are 19.0, 20.4, and 20.4 ppb in Huaibei, Hefei, and Tai'an, respectively. The mean $O_3$ concentration at 7:00 on $O_3$ exceedance days in Huaibei, Hefei, and Tai'an are 24.3, 33.7, and 34.2 ppb, respectively. More importantly, the differences in the $O_3$ growth rate between 8:00 and 14:00 under different $O_3$ pollution levels in Hefei, Huaibei, and Tai'an are even larger, with the mean $O_3$ growth rate on $O_3$ level 0 days being 2.4, 2.1, and 2.4 ppb/h, respectively, while the mean $O_3$ growth rate between 8:00 and 14:00 on $O_3$ exceedance days is 10.7, 9.6, and 10.1 ppb/h, respectively. The maximum $O_3$ growth rate in Hefei (14.8 ppb/h) and Huaibei (13.2 ppb/h) occurs at 10:00, and the maximum $O_3$ growth rate in Tai'an (13.2 ppb/h) occurs at 11:00. Therefore, Accumulation of the previous night's $O_3$ concentration and the rapid increase in $O_3$ concentration between 8:00 and 14:00 is the main reason for the $O_3$ exceedance.

Figure 3 shows the mean diurnal variations in the $NO_2$ vertical distributions at different $O_3$ pollution levels in Hefei, Huaibei, and Tai'an during April–October, 2020–2023. The diurnal variation in the $NO_2$ vertical distributions is essentially the same under different $O_3$ pollution levels. The $NO_2$ is mainly concentrated below 0.3 km, with high $NO_2$ concentrations in the morning. $NO_2$ photolysis occurs rapidly with an increase in sunlight intensity, and thus the $NO_2$ concentration usually reaches its lowest value in the afternoon (13:00–15:00) and then increases slightly in the early evening. Further investigation of the difference in the diurnal variation of $NO_2$ below 0.3 km on $O_3$ exceedance days and $O_3$ level 1 days reveals that the mean $NO_2$ concentrations in Hefei, Huaibei, and Tai'an at 8:00–9:00 on $O_3$ exceedance days are 1.22, 0.23, and 0.97 ppb higher than that on $O_3$ level 0 days, respectively. Moreover, the mean $NO_2$ concentrations below 0.3 km in Hefei, Huaibei, and Tai'an at 10:00–16:00 on $O_3$ exceedance days are 1.18, 1.61, and 1.60 ppb lower than that on $O_3$ level 0 days, respectively. This suggests that there is a greater accumulation of $NO_2$ as a raw material for

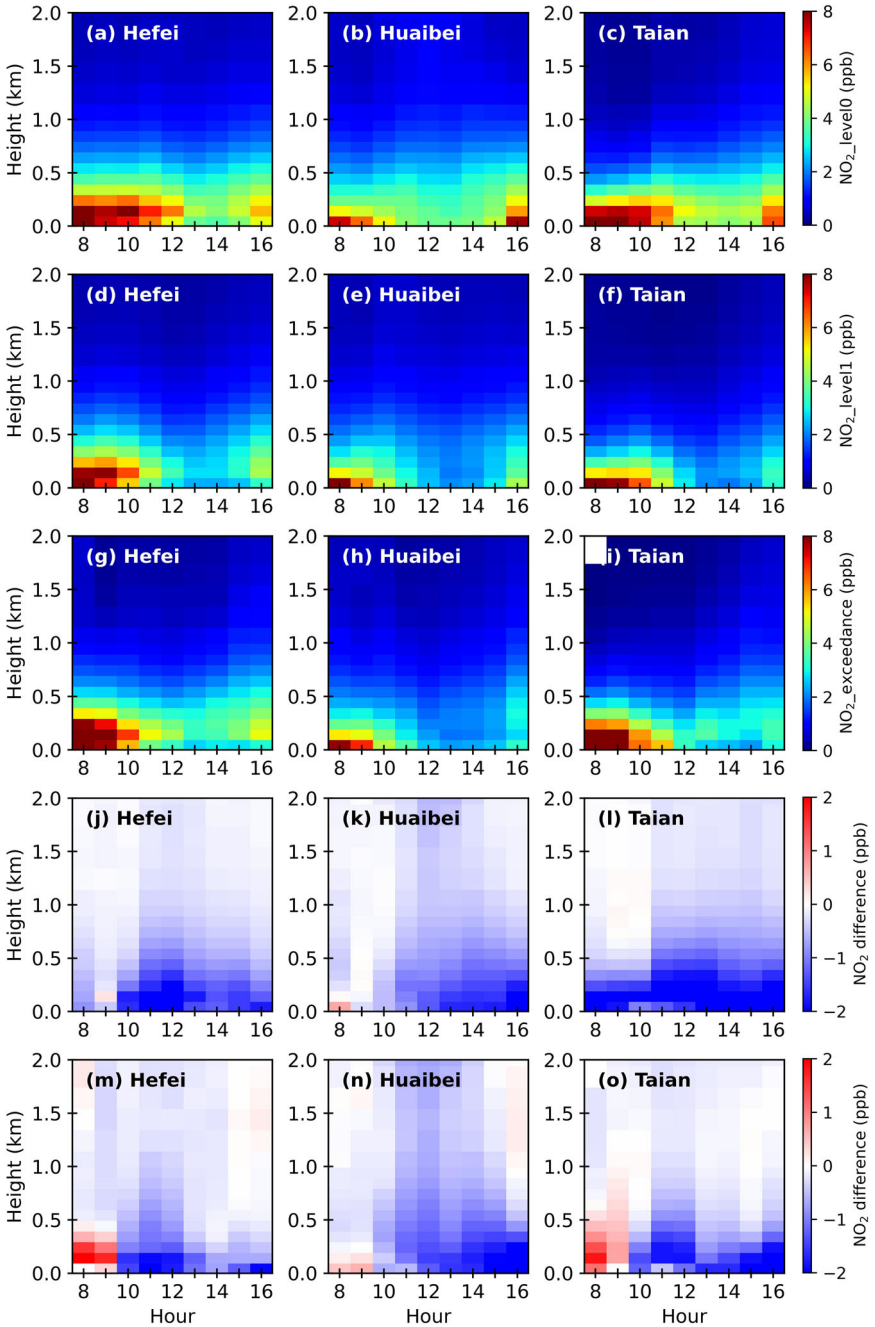


**Fig. 3 | Diurnal variations in the $NO_2$ vertical distributions.** Mean diurnal variations in the $NO_2$ vertical distributions on $O_3$ **a**–**c** level 0, **d**–**f** level 1, and **g**–**i** exceedance days in Hefei, Huaibei, and Tai'an during April–October, 2020–2023. Mean diurnal variations in the difference in $NO_2$ vertical distributions between $O_3$ level 1 days and $O_3$ level 0 days in **j** Hefei, **k** Huaibei, and **l** Tai'an during April–October, 2020–2023. Mean diurnal variations in the difference in $NO_2$ vertical distributions between $O_3$ exceedance days and $O_3$ level 0 days in **m** Hefei, **n** Huaibei, and **o** Tai'an during April–October, 2020–2023.

photochemical reactions in the early morning on $O_3$ exceedance days. In addition, more rapid photolysis of $NO_2$ occurs on $O_3$ exceedance days, resulting in a large amount of $O_3$ production. Meteorological conditions also support this conclusion, with higher downward ultraviolet radiation and temperature and lower relative humidity on $O_3$ exceedance days (Supplementary Figs. 3–5). These meteorological conditions are conducive to the photolysis of $NO_2$, resulting in lower $NO_2$ concentrations at noon and in the afternoon on $O_3$ exceedance days[34–37]. The $NO_2$ concentrations below 0.3 km in Hefei (0.43 ppb) and Tai'an (1.99 ppb) at 8:00–9:00 on $O_3$ level 1 days are lower than those on $O_3$ level 0 days, whereas the $NO_2$ concentration in Huaibei (0.03 ppb) is slightly increased. The $NO_2$ concentrations in Hefei, Huaibei, and Tai'an at 10:00–16:00 on $O_3$ level 1 days are significantly lower than those on $O_3$ level 0 days, which may also be related to meteorological conditions (higher downward ultraviolet radiation and temperature).

Significant increases in HCHO concentrations on $O_3$ exceedance days and $O_3$ level 1 days relative to those on $O_3$ level 0 days occur throughout the day (Fig. 4). The mean HCHO vertical profile on $O_3$ exceedance days is Gaussian in shape, with peaks typically occurring at altitudes of 0.1–0.3 km, which is caused by a combination of primary emissions of surface HCHO and photochemical oxidation processes at high altitudes. On average, the HCHO concentrations below 1.0 km on $O_3$ exceedance days in Hefei, Huaibei, and Tai'an are approximately 1.3–2.1, 1.1–2.0, and 1.6–2.6 times higher than those on $O_3$ level 0 days, respectively. There may be two reasons for the large difference between the HCHO concentrations on $O_3$ exceedance days and $O_3$ level 0 days. First, there is more secondary generation of HCHO in an $O_3$–rich environment[18], i.e., under favorable meteorological conditions (higher downward ultraviolet radiation and temperature, lower relative humidity), photooxidation of VOCs is promoted, thus increasing the HCHO concentration. Second, hot and dry conditions also promote natural emissions, e.g. vegetation emissions of VOCs[38], which further contribute to the increase in HCHO concentration.

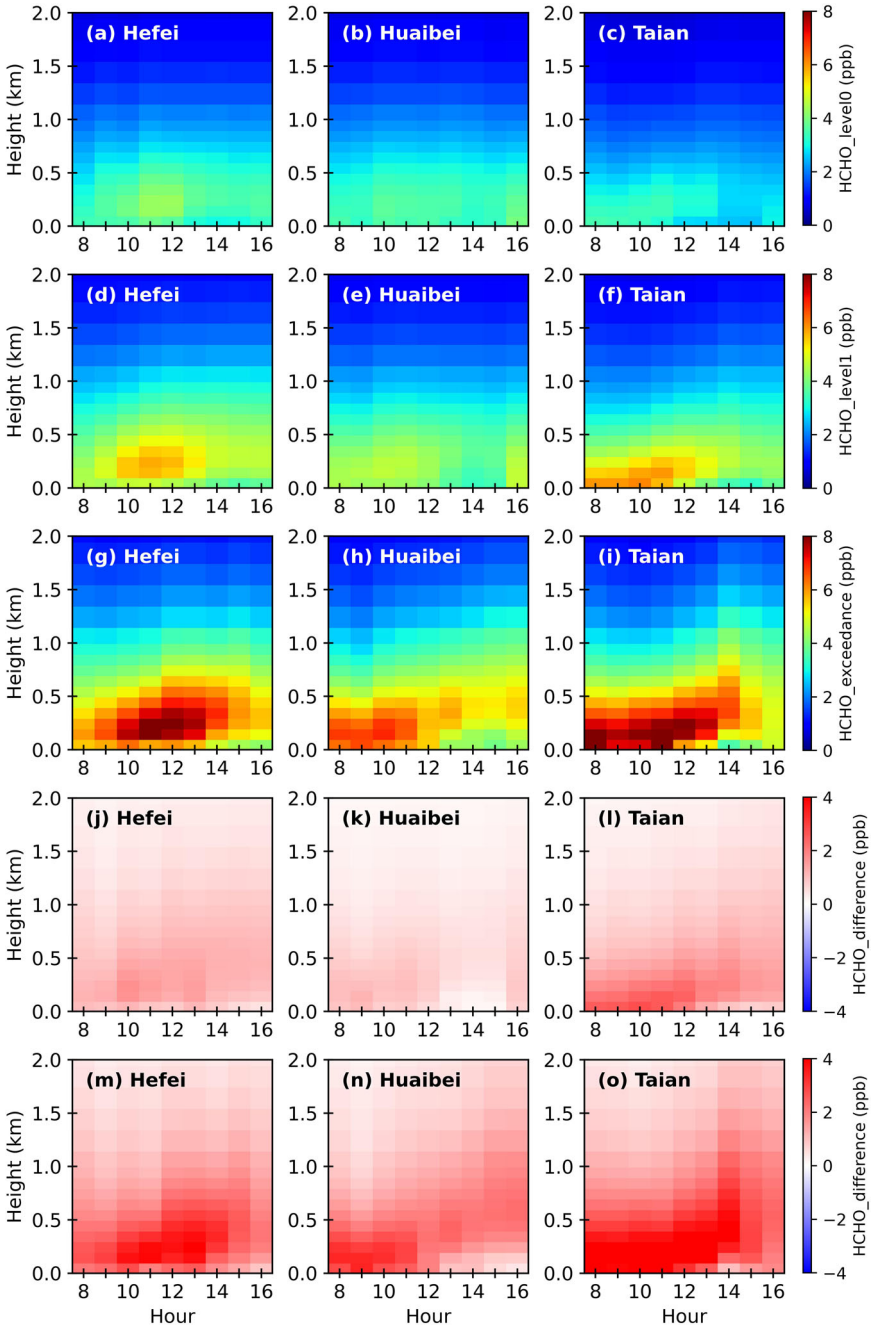


**Fig. 4 | Diurnal variations in the HCHO vertical distributions.** Mean diurnal variations in the HCHO vertical distributions on $O_3$ **a**–**c** level 0, **d**–**f** level 1, and **g**–**i** exceedance days in Hefei, Huaibei, and Tai'an during April–October, 2020–2023. Mean diurnal variations in the difference in HCHO vertical distributions between $O_3$ level 1 days and $O_3$ level 0 days in **j** Hefei, **k** Huaibei, and **l** Tai'an during April–October, 2020–2023. Mean diurnal variations in the difference in HCHO vertical distributions between $O_3$ exceedance days and $O_3$ level 0 days in **m** Hefei, **n** Huaibei, and **o** Tai'an during April–October, 2020–2023.

Therefore, abundant $O_3$ precursors (higher $NO_2$ and HCHO concentrations) are generally present in the early morning on $O_3$ exceedance days, and under favorable meteorological conditions, the rapid photolysis of $NO_2$ produces a large amount of $O_3$, causing the $NO_2$ concentration to decline rapidly and reach its lowest value near the surface in the afternoon. The secondary formation of HCHO in $O_3$–rich environments is more intense and reaches its maximum value at 0.1–0.3 km at noon. This result also indicates that $O_3$–rich environments may be more favorable for photochemical reactions at high altitudes. In addition, the diurnal variations in the $NO_2$ and HCHO concentrations are more drastic on $O_3$ exceedance days than on $O_3$ level 0 days.

### Vertical differences in ozone formation sensitivities under different ozone pollution levels

Figure 2 shows that the mean FNR vertical profile exhibits a Gaussian shape, with a peak occurring around 1.0–1.8 km. At lower altitudes (0–0.5 km), the estimated mean FNRs are lower than 2.5, indicating that the surface OFS is controlled by the VOC–limited regime. However, FNR is a diagnostic indicator of OFS that varies with time and height[18,19], and changes in long–term mean values usually cannot accurately reflect the transition of OFS with time and height. Therefore, based on the HCHO and $NO_2$ vertical profiles under different $O_3$ pollution levels, the occurrence probabilities of OFS at different heights in Hefei (Fig. 5), Huaibei (Supplementary Fig. 6), and Tai'an (Supplementary Fig. 7) during April–October 2020–2023 are classified and statistically analyzed. It is worth noting that the FNR here is derived using the hourly average $NO_2$ and HCHO, and the determination threshold (details refer to METHODS M4) is applied to determine the VOC–limited regime, transition limited regime, and $NO_x$–limited regime. Finally, the occurrence probabilities of the VOC–limited regime, transition limited regime, and $NO_x$–limited regime are determined at different altitudes and different periods.

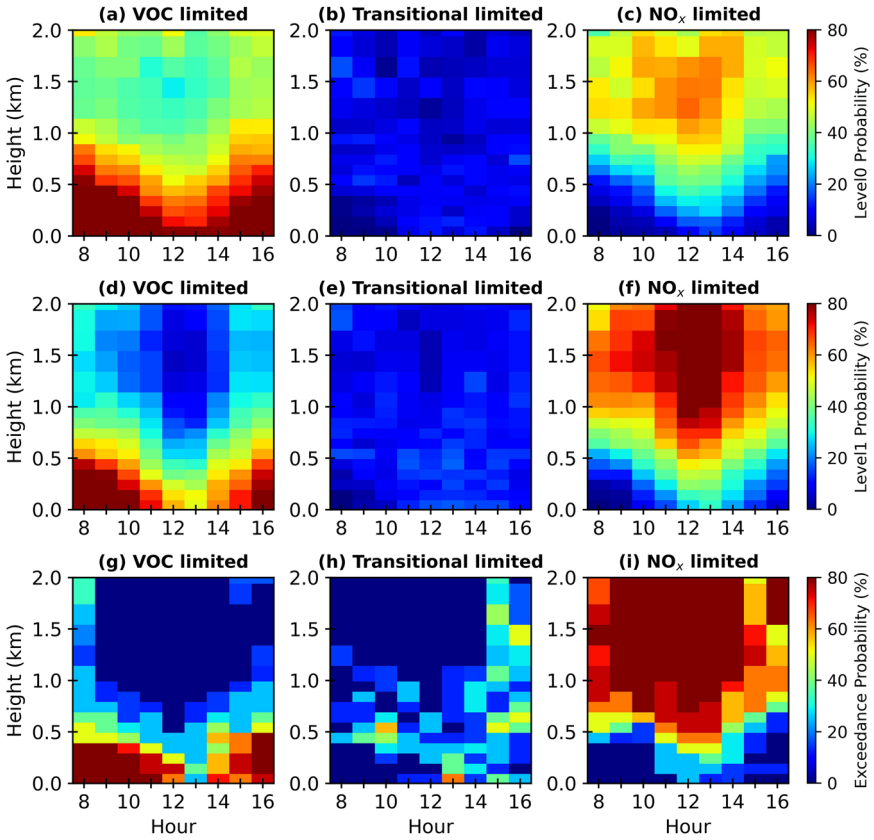


**Fig. 5 | Diurnal variations in the $O_3$ formation sensitivity.** Occurrence probability of diurnal variations in the **a** VOC-limited regime, **b** transition-limited regime, and **c** $NO_x$-limited regime vertical distributions on $O_3$ level 0 days; **d** VOC-limited regime, **e** transition-limited regime, and **f** $NO_x$-limited regime vertical distributions on $O_3$ level 1 days; and **g** VOC-limited regime, **h** transition-limited regime, and **i** $NO_x$-limited regime vertical distributions on $O_3$ exceedance days in Hefei during April–October, 2020–2023.

On $O_3$ level 0 days, the VOC–limited regime contributes most significantly to the surface OFS in Hefei (>79%), Huaibei (>67%), and Tai'an (>87%), and the contributions of the transition limited regime and $NO_x$–limited regime are less than 20% (Fig. 5, Supplementary Figs. 6, 7). With increasing altitude, the contribution of the VOC–limited regime gradually decreases, the contribution of the $NO_x$–limited regime increases, and the contribution of the transition limited regime remains almost constant. Above 1 km, the contribution of the VOC–limited regime reaches a minimum (approximately 28%, 27%, and 10% in Hefei, Huaibei, and Tai'an, respectively), and the contribution of the $NO_x$–limited regime reaches a maximum (approximately 64%, 67%, and 84% in Hefei, Huaibei, and Tai'an, respectively). Diurnally, the VOC–limited regime has the greatest contribution at 08:00 and 16:00 (more than 85% below 0.3 km in Hefei, Huaibei, and Tai'an), and the contributions of the transition limited regime (approximately 10%, 12%, and 5% below 0.3 km in Hefei, Huaibei, and Tai'an, respectively) and $NO_x$–limited regime (approximately 17%, 22%, and 10% below 0.3 km in Hefei, Huaibei, and Tai'an, respectively) increase at midday (12:00–14:00). Similarly, diurnal and vertical variations in the OFS have been observed in other cities in China[19,20].

The height–temporal evolution of the OFS occurrence probability on $O_3$ exceedance days and $O_3$ level 1 days is generally similar to that on $O_3$ level 0 days, but there are three differences (Fig. 5, Supplementary Figs. 6, 7). First, the contribution of the $NO_x$–limited regime at high altitudes increases significantly, particularly on $O_3$ exceedance days. The average contributions of the $NO_x$–limited regime within 0.5–2 km on $O_3$ level 1 days in Hefei, Huaibei, and Tai'an are 66%, 55%, and 78%, respectively. The average contributions of the $NO_x$–limited regime within 0.5–2 km on $O_3$ exceedance days in Hefei, Huaibei, and Tai'an are 77%, 78%, and 86%, respectively. Second, the average contributions of the surface transition limited regime and $NO_x$–limited regime increase at midday (12:00–14:00). The average contributions of the $NO_x$–limited regime (transition limited regime) on $O_3$ level 1 days in Hefei, Huaibei, and Tai'an are 27% (16%), 28% (21%), and 21% (21%), respectively, and the average contributions of the $NO_x$–limited regime (transition limited regime) on $O_3$ exceedance days in Hefei, Huaibei, and Tai'an are 17% (30%), 22% (16%), and 8% (16%), respectively. Third, the contribution of the transition limited regime increased significantly on $O_3$ exceedance days, particularly at 0.1–0.4 km at midday (12:00–14:00), with average contributions of the transition limited regime in Hefei, Huaibei, and Tai'an of 22%, 29%, and 30%, respectively. Overall, the occurrence probability of the VOC–limited regime decreases on $O_3$ exceedance days, while the occurrence probabilities of the transition limited regime and $NO_x$–limited regime increase, especially at high altitudes on $O_3$ exceedance days.

Furthermore, the OFS is generally in the VOC–limited regime on $O_3$ exceedance days during the period of a sharp rise in $O_3$ concentrations (8:00–12:00), and the contributions of the transition limited regime or $NO_x$–limited regime increases when the $O_3$ concentration peaks (12:00–14:00). Therefore, the reduction in the VOC concentrations is the key to reversing the current high $O_3$ levels, while control of the $NO_x$ concentration cannot be neglected to further reduce the peak $O_3$ concentration and number of $O_3$ exceedance days. When formulating $O_3$ control policies, it is important to consider diurnal and vertical variations in the OFS while addressing $O_3$ precursor emissions at different times. Measures such as vehicle restrictions and the adoption of renewable energy sources can be implemented at midday, and more stringent regulations of chemical plants are needed in the early morning and mid–morning to reduce the release of VOCs, e.g., by delaying the start–up time of chemical plants. The goal is to reduce VOC emissions during the period of a sharp rise in $O_3$ concentrations and reduce $NO_x$ emissions at midday and afternoon based on the primary OFS regime during these times.

### Spatial differences in ozone formation sensitivities under different ozone pollution levels

Figure 6 shows the occurrence probabilities of the VOC–limited regime, transition limited regime, and $NO_x$–limited regime spatial distributions derived from TROPOMI observations under different $O_3$ pollution levels in

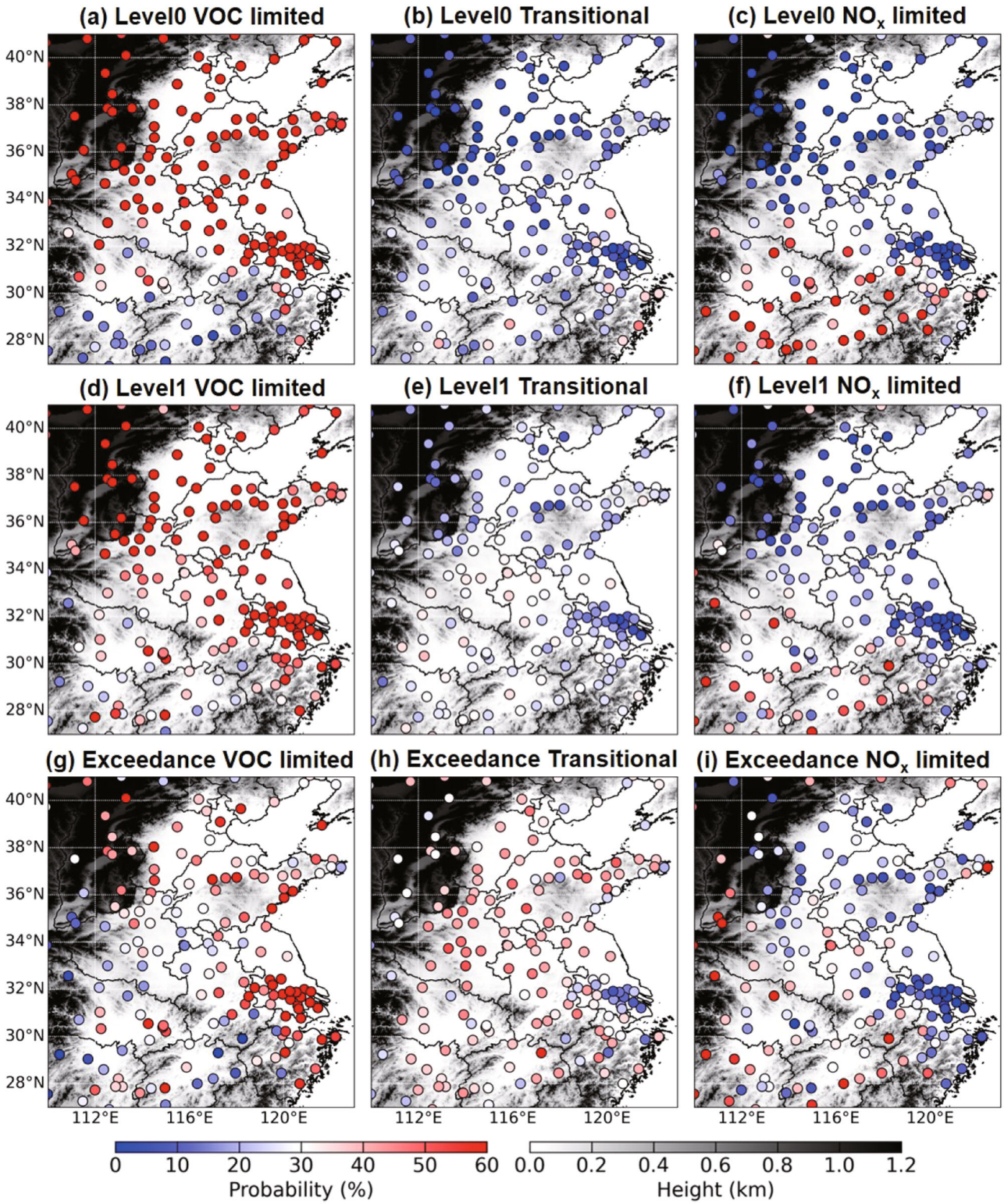


**Fig. 6 | Spatial distribution of $O_3$ formation sensitivity.** Occurrence probabilities of the **a** VOC-limited regime, **b** transition-limited regime, and **c** $NO_x$-limited regime spatial distributions on $O_3$ level 0 days; **d** VOC-limited regime, **e** transition-limited regime, and **f** $NO_x$-limited regime spatial distributions on $O_3$ level 1 days; and **g** VOC-limited regime, **h** transition-limited regime, and **i** $NO_x$-limited regime spatial distributions on $O_3$ exceedance days in eastern Chinese cities derived by TROPOMI observations during April–October, 2020–2023.

eastern China during April–October, 2020–2023. The OFS of most cities in the NCP and MLYRP is mainly in the VOC–limited regime on $O_3$ level 0 days, whereas the OFS of most cities in the southeast hills is mainly in the $NO_x$–limited regime on $O_3$ level 0 days. On $O_3$ level 1 days, the occurrence probability of the VOC–limited regime decreases for most cities in the NCP and MLYRP, whereas the contribution of the $NO_x$–limited regime decreases in most cities in the southeastern hills, and this trend is more significant on $O_3$ exceedance days. The regional mean contributions of the VOC–limited

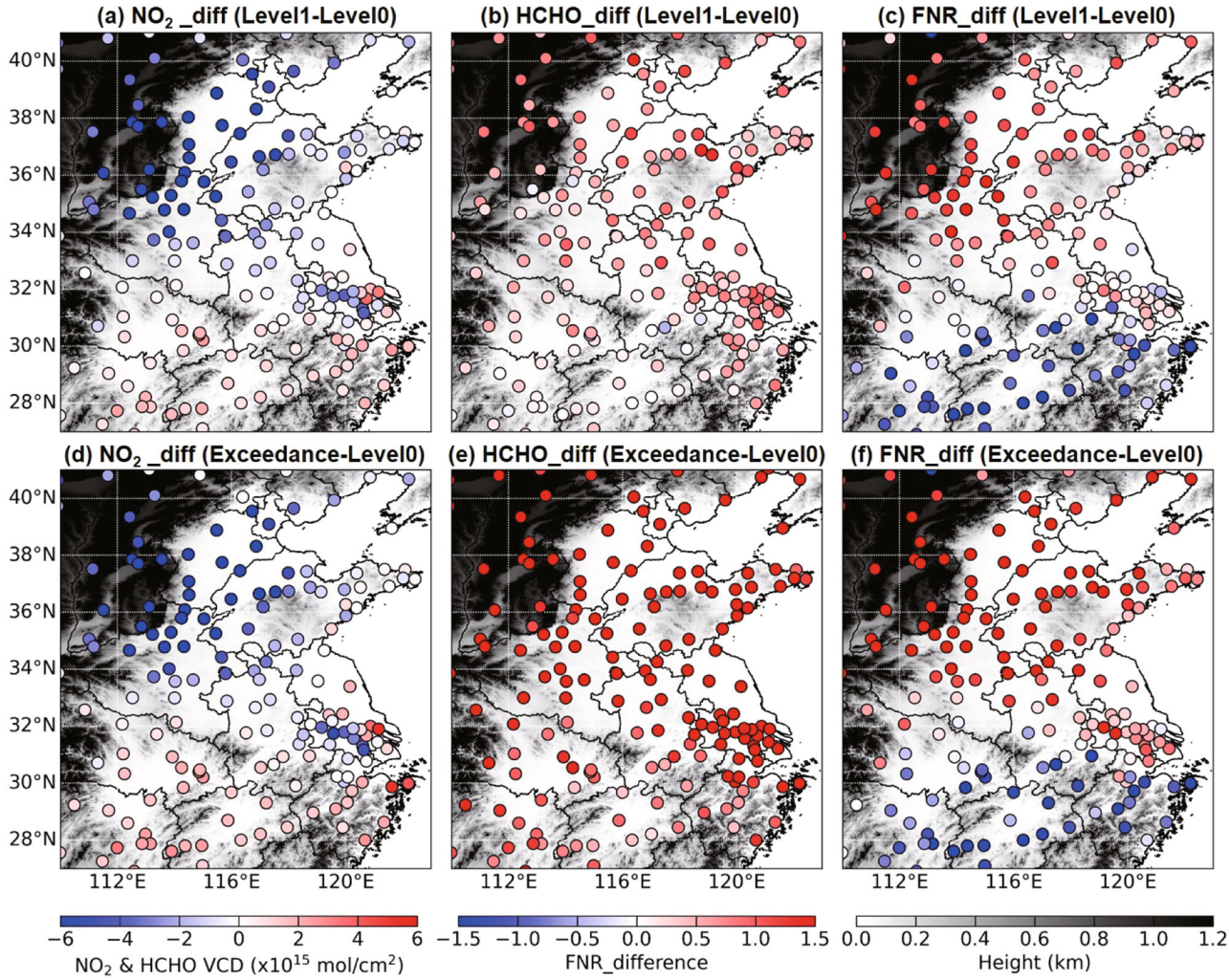


**Fig. 7 | Spatial distributions of the difference in $O_3$ precursors.** Spatial distributions of the difference in tropospheric **a** $NO_2$ VCD, **b** HCHO VCD, and **c** FNR between $O_3$ level 1 days and $O_3$ level 0 days, and the difference in tropospheric **d** $NO_2$ VCD, **e** HCHO VCD, and **f** FNR between $O_3$ exceedance days and $O_3$ level 0 days in eastern China during April–October, 2020–2023.

regime, transition limited regime, and $NO_x$–limited regime on $O_3$ level 0 days in the NCP (MLYRP) are 83% (72%), 10% (15%), and 7% (14%), respectively. The regional mean contribution of the VOC–limited regime in the NCP (MLYRP) decrease to 39% (63%) on $O_3$ exceedance days, and the regional mean contribution of the transition limited regime in the NCP (MLYRP) increases to 38% (26%) on $O_3$ exceedance days. On $O_3$ level 0 days, the regional mean contributions of the VOC–limited regime, transition limited regime, and $NO_x$–limited regime in the southeastern hilly region are 18%, 24%, and 58%, respectively. On $O_3$ exceedance days, the regional mean contribution of the $NO_x$–limited regime in the southeastern hilly region decreases to 34%, and the regional mean contribution of the transition limited regime increases to 35%. Therefore, targeted $O_3$ control measures are necessary for different regions. VOC emissions control should mainly focus on most cities in the NCP and MLYRP, and a possible recommendation is to avoid planting trees with high VOC emissions[21], such as poplars, pines, and abies, in areas with high $NO_x$ emissions, such as roadsides and power plants. However, $NO_x$ emissions control should be mainly concentrated in the cities in the southeastern hills.

The shift in OFS at different $O_3$ pollution levels may depend mainly on the photochemical conditions and emission characteristics of $O_3$ precursors. Figure 7a, d shows the differences in $NO_2$ concentrations observed by TROPOMI. $NO_2$ is lower in most cities in the NCP on $O_3$ level 1 days and $O_3$ exceedance days relative to $O_3$ level 0 days (Supplementary Fig. 8), because high temperatures and strong ultraviolet radiation are necessary for high $O_3$ concentrations, and these favorable meteorological conditions are more conducive to the photolysis reaction of $NO_2$. In contrast, $NO_2$ concentrations in most cities in the southeastern hills increase on $O_3$ level 1 days and $O_3$ exceedance days compared with the $NO_2$ concentrations on $O_3$ level 0 days. Most cities in the southeastern hills are under the $NO_x$–limited regime; thus, a high $NO_2$ concentration is a necessary condition for inducing high $O_3$ concentrations. A significant limitation of the TROPOMI observations is its inability to capture diurnal variations in air pollutant concentrations. Here, we further analyze the spatial distribution of surface $NO_2$ concentrations measured by Ministry of Ecology and Environment of China (MEE) in eastern China (Supplementary Figs. 9, 10). Consistent with the MAX–DOAS measurements, the $NO_2$ concentration is considerably higher in most cities in eastern China in the early morning on $O_3$ level 1 days and $O_3$ exceedance days than the $NO_2$ concentrations on $O_3$ level 0 days. Under favorable meteorological conditions (higher downward ultraviolet radiation and temperature and lower relative humidity), the rapid photolysis of $NO_2$ in the morning leads to a rapid decrease in $NO_2$ concentrations and a rapid increase in $O_3$ concentrations in the late afternoon.

The differences in HCHO concentrations under different $O_3$ pollution levels are also consistent with the MAX–DOAS measurements, where favorable meteorological conditions on $O_3$ level 1 days and $O_3$ exceedance days enhance the photochemical reactions and increase the secondary HCHO concentrations as well as the emission of biogenic VOCs from vegetation. It is worth noting that the FNR values of most cities in the NCP

and MLYRP on $O_3$ level 1 days and $O_3$ exceedance days increase compared with those on $O_3$ level 0 days, whereas the FNR values of most cities in the southeastern hills on $O_3$ level 1 days and $O_3$ exceedance days decrease compared with those on $O_3$ level 0 days. Therefore, the difference in FNR values between northern and southern cities in eastern China on $O_3$ exceedance days narrows, and the OFS tends to be higher in the transition limited regime (Fig. 6h). This also implies that although there is a difference in the importance of $O_3$ precursor emission control targets ($NO_x$ in the south and VOCs in the north) between northern and southern cities in eastern China, this does not mean that controlling only one of the precursors can achieve the best effect of $O_3$ prevention, and the most appropriate ratio of $O_3$ precursor emission reduction should be designed according to different regions.

## Discussion

Owing to the limitations of the observational data, the analysis of vertical differences in $O_3$ precursors and OFS under different $O_3$ pollution levels is limited to three cities in eastern China. Although other cities in eastern China were further investigated using satellite observations, TROPOMI only provides observation results for column concentrations at approximately 13:30 each day, which did not allow us to obtain diurnal and vertical variations in the OFS. Further observations must be extended to southern and coastal cities to investigate the relationship between $O_3$ and its precursors more comprehensively. For example, Wang et al.[39] found that, driven by weather systems and mesoscale recirculation, the interaction between continental and marine air masses profoundly altered the atmospheric composition, which further affected the formation and redistribution of $O_3$ in coastal areas, resulting in a significant difference in the photochemical processes of $O_3$ between coastal and inland areas. When continental air intrudes into the marine atmosphere, $O_3$ pollution at sea is amplified, and the elevated $O_3$ will be recirculated to the coast near the shore by the sea breeze, resulting in increased $O_3$ pollution in coastal cities. Another limitation of the study is that we used fixed FNR thresholds at different heights, a fixed threshold may underestimate the contribution of upper layer VOC–limited regime and overestimate the contribution of upper layer $NO_x$–limited regime according to previous investigation[20]. In the future, OFS can be further diagnosed using height–dependent FNR thresholds to obtain more accurate results.

By combining ground–and satellite–based hyperspectral remote sensing with ground station observations, this study investigated the vertical and spatial features and differences in the OFS in eastern Chinese cities under different ambient $O_3$ levels. The diurnal trends in the $NO_2$ and HCHO vertical distributions were similar under different $O_3$ pollution levels. The $NO_2$ concentration was mainly concentrated below 0.3 km, with high $NO_2$ concentrations in the morning. Compared with the $O_3$ level 0 days, there was more accumulation of $NO_2$ as a raw material for photochemical reactions in the early morning on $O_3$ exceedance days, and more rapid photolysis of $NO_2$ occurred on $O_3$ exceedance days, resulting in a large amount of $O_3$ production. The mean HCHO vertical profile under different $O_3$ pollution levels was Gaussian in shape, with peaks typically occurring at altitudes of 0.1–0.3 km; compared with $O_3$ level 0 days, the HCHO concentration was higher throughout the day on $O_3$ exceedance days.

There were also significant differences in the OFS under different $O_3$ pollution levels. The contribution of the $NO_x$–limited regime at high altitudes increased significantly on $O_3$ exceedance days compared with that on $O_3$ level 0 days. In addition, the contribution of the transition limited regime also increased significantly on $O_3$ exceedance days, particularly at 0.1–0.4 km at midday (12:00–14:00). Furthermore, the OFS was generally in the VOC–limited regime on $O_3$ exceedance days during the period of a sharp rise in $O_3$ concentrations (8:00–12:00), and the contributions of the transition limited regime or $NO_x$–limited regime increased when the $O_3$ concentration peaked (12:00–14:00). Therefore, reducing the VOC concentrations is the key to reversing the current high $O_3$ levels, while controlling $NO_x$ concentrations cannot be neglected to further reduce the peak $O_3$ concentration and the number of $O_3$ exceedance days. Spatially, the OFS of most cities in the NCP and MLYRP was mainly in the VOC–limited regime on $O_3$ level 0 days, whereas the OFS of most cities in the southeastern hills was mainly in $NO_x$–limited regime on $O_3$ level 0 days. On $O_3$ level 1 days and $O_3$ exceedance days, the difference in FNR values between northern and southern cities in eastern China on $O_3$ exceedance days narrowed, the occurrence probability of the VOC–limited regime decreased for most cities in the NCP and MLYRP, the contribution of the $NO_x$–limited regime of most cities in the southeastern hills decreased, and the OFS in eastern China tended to be under a transition limited regime.

## Methods

### M1 MAX–DOAS measurements

The ground–based MAX–DOAS stereo remote sensing network was continuously measured from December 22, 2020, to May 15, 2023; April 12, 2019, to May 27, 2022; and July 15, 2021, to May 15, 2023, in Hefei, Huaibei, and Tai'an, respectively. The three cities transition sequentially from south to north (Fig. 1a) to obtain the vertical profiles of $O_3$ precursors in eastern China. The MAX–DOAS instrument consists of a telescope, two spectrometers, and a controlling computer. MAX–DOAS obtains trace gas vertical profiles from scattered sunlight observed at different elevation angles, with a complete scan lasting approximately 12 min. The system operates only during the daytime (08:00–16:00 local time) with a temporal resolution of 15 min, a spatial resolution of 100 m for altitudes up to 1 km, and a spatial resolution of 200 m for altitudes of 1–2 km. Detailed information regarding the $NO_2$ and HCHO vertical profile retrieval algorithms and their validation can be found in our previous studies[40–43].

In addition, we compared the surface $NO_2$ concentrations observed by the MAX–DOAS with the urban surface $NO_2$ concentrations measured by the MEE (Supplementary Fig. 11), and the results were comparable to those reported in previous studies[19,44], with Pearson's correlation coefficients for Hefei, Huaibei, and Tai'an of 0.74 ($P < 0.01$), 0.66 ($P < 0.01$), and 0.73 ($P < 0.01$), respectively. Therefore, the MAX–DOAS retrieval is considered reliable. The differences between the MAX–DOAS and MEE observations arise from two components. First, the detection modes differ: the urban $NO_2$ concentration observed by MAX–DOAS is the result of scanning along a fixed direction, whereas the urban $NO_2$ concentration observed by MEE is the result of in situ sampling. Second, there are some differences in the observation locations, as the urban $NO_2$ concentration from the MEE is the average of several in situ stations, whereas only one MAX–DOAS observation site is equipped in each city.

### M2 Surface measurements

In this study, we investigated the OFS in 156 cities in eastern China. The spatial distribution of these 156 cities is shown in Fig. 1c. The data for the MDA8O3, hourly $O_3$ concentration, and hourly $NO_2$ concentration in 156 cities from April to October in 2020–2023 were obtained from the MEE open access website, https://www.mee.gov.cn (last accessed: July 7, 2024) and archived at https://quotsoft.net/air/ (last accessed: July 7, 2024). After August 31, 2018, the MEE reported a concentration unit of $\mu g/m^3$ at the reference state (298 K, 1013 hPa), and the mass concentrations ($\mu g/m^3$) at each site were converted to volume mixing ratios (VMRs, ppb). To explore the $O_3$ formation sensitivities under different $O_3$ pollution levels, the entire observation period was classified into $O_3$ level 0 days (clean days, MDA8O3 < 100 $\mu g/m^3$), $O_3$ level 1 days (light pollution days, 100 $\mu g/m^3$ < MDA8O3 < 160 $\mu g/m^3$), and $O_3$ exceedance days (heavy pollution days, MDA8O3 > 160 $\mu g/m^3$) according to the "China Ambient Air Quality Index Technical Regulations (Trial)" (HJ633–2012) standard (Supplementary Table 1). To discuss the differences in the $O_3$ formation sensitivities under different $O_3$ pollution levels, the $O_3$ precursor concentration on $O_3$ level 0 days was used as a reference, and the differences in the $O_3$ precursor concentrations under different $O_3$ pollution levels were defined as the $O_3$ precursor concentration on $O_3$ level 1 days minus the $O_3$ precursor concentration on $O_3$ level 0 days, and the $O_3$ precursor concentration on $O_3$ exceedance days minus the $O_3$ precursor concentration on $O_3$ level 0 days.

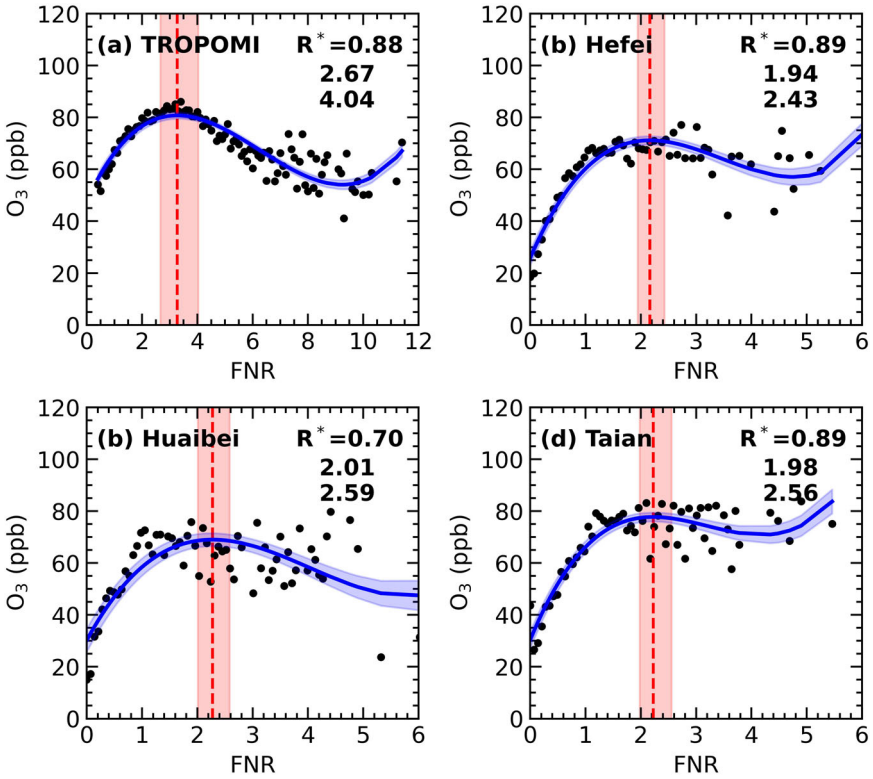


**Fig. 8 | Diagnosing the $O_3$ formation sensitivity.** Fitting of **a** MEE-observed surface monthly mean $O_3$ concentrations as a function of the binned FNR measured by TROPOMI during April–October, 2020–2023. Fitting of the MEE-observed surface hourly mean $O_3$ concentrations as a function of the binned FNR measured by MAX–DOAS in **b** Hefei, **c** Huaibei, and **d** Tai'an. The solid blue line represents the third-order polynomial fitting, and the blue shadow represents the 95% confidence band. The correlation coefficients are shown at the top right of each panel, and the superscript asterisk indicates $P < 0.01$. The vertical red dotted line represents the maximum value of the fitted curve, and the vertical red shadow represents the range of the curve slope from −3 to +3 (transition regime). The area to the left of the red shading is the VOC-limited regime and the area to the right is the $NO_x$-limited regime. The labels at the top right of each panel represent the threshold values for the $NO_x$-limited regime (high) and VOC-limited regime (low).

### M3 Satellite observations

The TROPOMI onboard the European Space Agency's Copernicus Sentinel 5 precursor satellite can provide daily global coverage of HCHO and $NO_2$ vertical column density (VCD) observations[45–47]. TROPOMI has a high spatial resolution of 3.5 × 7.0 km and an overpass of approximately 13:30. In this study, TROPOMI $NO_2$ ("S5P_OFFL_L2__NO2…") and HCHO ("S5P_OFFL_L2__HCHO…") tropospheric VCD products from April to October 2020–2023 were employed[48] (downloaded from https://search.earthdata.nasa.gov/search; Last visited: January 7, 2024). The recommended quality control (QC, in the 0–1 range) filter was used, and HCHO retrieval values with QC values less than 0.5 and $NO_2$ retrieval values with QC values less than 0.75 were excluded. To match the $O_3$ concentrations measured at the MEE sites, we averaged the TROPOMI observations (HCHO and $NO_2$ tropospheric VCDs) over a range of 0.2° at the surface MEE urban stations.

The $NO_2$ and HCHO tropospheric VCDs measured using MAX–DOAS and TROPOMI were also compared. Considering the TROPOMI satellite transit time of around 13:30, the mean MAX–DOAS values from 13:00–14:00 were used for comparison. The TROPOMI observations were averaged over a range of 0.2° at the ground–based MAX–DOAS station. Comparisons of the tropospheric VCDs of $NO_2$ and HCHO observed by MAX–DOAS and TROPOMI are shown in Supplementary Figs. 12 and 13. In general, the MAX–DOAS and TROPOMI observations are relatively consistent, with Pearson correlation coefficients of 0.99 (0.74), 0.96 (0.66), and 0.96 (0.73) for $NO_2$ (HCHO) in Hefei, Huaibei, and Tai'an, respectively. The difference in comparisons between MAX–DOAS and TROPOMI observations can be caused by many factors, such as different observation modes, pixel size, fitting errors, a priori model bias, cloud and aerosols, and spatio–temporal resolution[48].

### M4 Diagnosing the ozone formation sensitivity

Based on the monthly mean surface midday (13:00–14:00) $O_3$ concentration observed by MEE in 156 cities in eastern China from April to October 2020–2023, and the monthly mean HCHO and $NO_2$ tropospheric VCDs observed by TROPOMI during the same period, the OFS was determined using the method proposed by Jin et al.[49] and Ren et al.[14] to derive FNR thresholds for transition limited regimes. The data were arranged according to the order of FNR values from small to large, forming bins at intervals of 0.1. Then, the $O_3$ concentration of the grouping was plotted as a function of the grouping FNR. $O_3$ initially increased and then decreased with an increase in FNR. Therefore, a polynomial rather than a linear function was used to fit the FNR curve. We used the third–order polynomial model to derive the maximum average $O_3$ concentration (peak of the curve in Fig. 8a). Assuming that the peak of the curve (where the curve slope is 0) marks the transition from a VOC–limited regime to a $NO_x$–limited regime, the transition zone (transition limited regime) was defined as the range of the curve with slopes between -3 and +3. Figure 8a summarizes all of the available observations and examines their empirical relationships with the observations of all cities in eastern China. It is found that the $O_3$ peaks at FNR = 3.31 and the transition limited regime ranges from 2.67 to 4.04. Therefore, based on the TROPOMI observations, we roughly defined the following three states: FNR < 2.67 is the VOC–limited regime; FNR > 4.04, is the $NO_x$–limited regime; 2.67 < FNR < 4.04 represents a transition limited regime. This result is similar to that of a recent study reporting FNR thresholds for major cities in China, which recommended FNR values between 2.3 and 4.2 as a transition limited regime[50].

Based on MEE–observed surface hourly $O_3$ concentrations, MAX–DOAS retrieved the HCHO and $NO_2$ profiles, and a similar approach was used to determine the FNR thresholds. First, the hourly averages of the surface HCHO and $NO_2$ concentrations observed by MAX–DOAS were used to match the $O_3$ concentrations observed by the MEE. The available observational values in Hefei, Huaibei, and Tai'an from April to October 2020–2023 were then summarized, and bins were formed at intervals of 0.1 according to the FNR values arranged in order from small to large. Finally, the grouping $O_3$ concentration was plotted as a function of the grouping FNR, and the third–order polynomial fitting is shown in Fig. 8b–d. The thresholds for the transition limited regime of Hefei, Huaibei, and Tai'an were 1.94–2.43, 2.01–2.59, and 1.98–2.56, respectively. In addition, we hypothesised that the FNR thresholds for determining the OFS would not change markedly with height by referring to recent studies by Liu et al.[51],

Lin et al.[19], and Hong et al.[18], because the limitations of our research, the retrieval of the ozone profile cannot be realized[52].

## Data availability

No datasets were generated or analysed during the current study.

Received: 29 August 2024; Accepted: 27 November 2024;
Published online: 23 January 2025

## References

1. Zhai, S. et al. Fine particulate matter (PM2.5) trends in China, 2013–2018: separating contributions from anthropogenic emissions and meteorology. *Atmos. Chem. Phys.* **19**, 11031–11041 (2019).
2. Zheng, B. et al. Trends in China's anthropogenic emissions since 2010 as the consequence of clean air actions. *Atmos. Chem. Phys.* **18**, 14095–14111 (2018).
3. Li, K. et al. Anthropogenic drivers of 2013–2017 trends in summer surface ozone in China. *Proc. Natl. Acad. Sci.* **116**, 422–427 (2018).
4. Li, K. et al. Ozone pollution in the North China Plain spreading into the late-winter haze season. *Proc. Natl. Acad. Sci*. **118**, https://doi.org/10.1073/pnas.2015797118 (2021).
5. Li, K. et al. Increases in surface ozone pollution in China from 2013 to 2019: anthropogenic and meteorological influences. *Atmos. Chem. Phys.* **20**, 11423–11433 (2020).
6. Chu, W. et al. Research on ozone formation sensitivity based on observational methods: Development history, methodology, and application and prospects in China. *J. Environ. Sci-China* **138**, 543–560 (2024).
7. Liu, C. & Shi, K. A review on methodology in O3-NOx-VOC sensitivity study. *Environ. Pollut*. **291**, https://doi.org/10.1016/j.envpol.2021.118249 (2021).
8. Sillman, S. The relation between ozone, NOx and hydrocarbons in urban and polluted rural environments. *Atmos. Environ.* **33**, 1821–1845 (1999).
9. Guo, J. et al. Evolution of ozone pollution in China: What track will it follow? *Environ. Sci. Technol.* **57**, 109–117 (2022).
10. Qu, H., Wang, Y., Zhang, R. & Li, J. Extending ozone-precursor relationships in China from peak concentration to peak time. *J. Geophys. Res-atmos*. **125**, https://doi.org/10.1029/2020jd033670 (2020).
11. Sillman, S. The use of NOy, H2O2, and HNO3 as indicators for ozone-NO x-hydrocarbon sensitivity in urban locations. *J. Geophys. Res-atmos.* **100**, 14175–14188 (1995).
12. Hong, Q. et al. Evaluating the feasibility of formaldehyde derived from hyperspectral remote sensing as a proxy for volatile organic compounds. *Atmos. Res*. **264**, https://doi.org/10.1016/j.atmosres.2021.105777 (2021).
13. Martin, R. V. et al. Evaluation of GOME satellite measurements of tropospheric NO2 and HCHO using regional data from aircraft campaigns in the southeastern United States. *J. Geophys. Res-atmos*. **109**, https://doi.org/10.1029/2004jd004869 (2004).
14. Ren, J., Guo, F. & Xie, S. Diagnosing ozone–NOx–VOC sensitivity and revealing causes of ozone increases in China based on 2013–2021 satellite retrievals. *Atmos. Chem. Phys.* **22**, 15035–15047 (2022).
15. Ren, B. et al. Vertical characteristics of NO2 and HCHO, and the ozone formation regimes in Hefei, China. *Sci. Total Environ*. **823**, https://doi.org/10.1016/j.scitotenv.2022.153425 (2022).
16. Tanvir, A. et al. Vertical Characteristics of HCHO and NO2 in Suburban Shanghai: Understanding of Ozone formation sensitivity via Secondary HCHO. *Environ. Res. Lett*., https://doi.org/10.1088/1748-9326/ad2d3c (2024).
17. Xue, J. et al. Identification of ozone sensitivity for NO2 and secondary HCHO based on MAX-DOAS measurements in northeast China. *Environ. Int*. **160**, https://doi.org/10.1016/j.envint.2021.107048 (2022).
18. Hong, Q. et al. Inferring vertical variability and diurnal evolution of O3 formation sensitivity based on the vertical distribution of summertime HCHO and NO2 in Guangzhou, China. *Sci. Total Environ*. **827**, https://doi.org/10.1016/j.scitotenv.2022.154045 (2022).
19. Lin, H. et al. Diagnosis of Ozone Formation Sensitivities in Different Height Layers via MAX-DOAS Observations in Guangzhou. *J. Geophys. Res-atmos*. **127**, https://doi.org/10.1029/2022jd036803 (2022).
20. Hu, Q. et al. Vertical evolution of ozone formation sensitivity based on synchronous vertical observations of ozone and proxies for its precursors: Implications for ozone pollution prevention strategies. *Environ. Sci. Technol.* **58**, 4291–4301 (2024).
21. Peng, H. et al. Studies on regional ozone formation sensitivities and transport with higher spatiotemporal resolutions in a stereoscopic dimension: GEMS and vertical observations. *Atmos. Res*. **302**, https://doi.org/10.1016/j.atmosres.2024.107314 (2024).
22. Zhang, X. et al. First long-term surface ozone variations at an agricultural site in the North China Plain: Evolution under changing meteorology and emissions. *Sci. Total Environ.* **860**, 160520 (2023).
23. Wei, X. L., Li, Y. S., Lam, K. S., Wang, A. Y. & Wang, T. J. Impact of biogenic VOC emissions on a tropical cyclone-related ozone episode in the Pearl River Delta region, China. *Atmos. Environ.* **41**, 7851–7864 (2007).
24. Fu, T. M. et al. Space-based formaldehyde measurements as constraints on volatile organic compound emissions in east and south Asia and implications for ozone. *J. Geophys. Res-atmos*. **112**, https://doi.org/10.1029/2006jd007853 (2007).
25. Zhu, S. et al. Spatiotemporal Variations in Satellite-Based Formaldehyde (HCHO) in the Beijing-Tianjin-Hebei Region in China from 2005 to 2015. *Atmos*. **9**, https://doi.org/10.3390/atmos9010005 (2018).
26. Lu, X. et al. Exploring 2016–2017 surface ozone pollution over China: source contributions and meteorological influences. *Atmos. Chem. Phys.* **19**, 8339–8361 (2019).
27. Kang, Y. et al. Evaluation and Evolution of MAX-DOAS-observed Vertical NO2 Profiles in Urban Beijing. *Adv. Atmos. Sci.* **38**, 1188–1196 (2021).
28. Kumar, V. et al. Long-term MAX-DOAS measurements of NO2, HCHO, and aerosols and evaluation of corresponding satellite data products over Mohali in the Indo-Gangetic Plain. *Atmos. Chem. Phys.* **20**, 14183–14235 (2020).
29. Lu, C. et al. Identification of O3 Sensitivity to Secondary HCHO and NO2 Measured by MAX-DOAS in Four Cities in China. *Remote Sens*. **16**, https://doi.org/10.3390/rs16040662 (2024).
30. Chan, K. L. et al. MAX-DOAS measurements of tropospheric NO2 and HCHO in Nanjing and a comparison to ozone monitoring instrument observations. *Atmos. Chem. Phys.* **19**, 10051–10071 (2019).
31. Ding, J. et al. Impacts of meteorology and precursor emission change on O3 variation in Tianjin, China from 2015 to 2021. *J. Environ. Sci-China* **126**, 506–516 (2023).
32. Fu, W. et al. Recent-year variations in O3 pollution with high-temperature suppression over central China. *Environ. Pollut*. **349**, https://doi.org/10.1016/j.envpol.2024.123932 (2024).
33. Li, K. et al. Large variability of O3-precursor relationship during severe ozone polluted period in an industry-driven cluster city (Zibo) of North China Plain. *J. Clean. Prod*. **316**, https://doi.org/10.1016/j.jclepro.2021.128252 (2021).
34. Kou, W. et al. High downward surface solar radiation conducive to ozone pollution more frequent under global warming. *Sci. Bull.* **68**, 388–392 (2023).
35. Nguyen, D.-H. et al. Tropospheric ozone and NOx: A review of worldwide variation and meteorological influences. *Environ. Technol*. **28**, https://doi.org/10.1016/j.eti.2022.102809 (2022).
36. Zhao, S. et al. Photolysis rate in the Beijing-Tianjin-Hebei region: Reconstruction and long-term trend. *Atmos. Res*. **256**, https://doi.org/10.1016/j.atmosres.2021.105568 (2021).

37. Zhao, S. et al. The influence of aerosols on the NO2 photolysis rate in a suburban site in North China. *Sci. Total Environ.* **767**, 144788 (2021).
38. Churkina, G. et al. Effect of VOC emissions from vegetation on air quality in Berlin during a heatwave. *Environ. Sci. Technol.* **51**, 6120–6130 (2017).
39. Wang, H. et al. Ozone pollution around a coastal region of South China Sea: interaction between marine and continental air. *Atmos. Chem. Phys.* **18**, 4277–4295 (2018).
40. Xing, C. et al. Vertical distributions and potential sources of wintertime atmospheric pollutants and the corresponding ozone production on the coast of Bohai Sea. *J. Environ. Manage*. **319**, https://doi.org/10.1016/j.jenvman.2022.115721 (2022).
41. Xing, C. et al. Observations of the vertical distributions of summertime atmospheric pollutants and the corresponding ozone production in Shanghai, China. *Atmos. Chem. Phys.* **17**, 14275–14289 (2017).
42. Liu, C. et al. Stereoscopic hyperspectral remote sensing of the atmospheric environment: Innovation and prospects. *Earth-Sci. Rev*. **226**, https://doi.org/10.1016/j.earscirev.2022.103958 (2022).
43. Liu, C. et al. Ground-based hyperspectral stereoscopic remote sensing network: A promising strategy to learn coordinated control of O3 and PM2.5 over China. *Engineering* **19**, 71–83 (2022).
44. Wang, Z. et al. Elevated dust layers inhibit dissipation of heavy anthropogenic surface air pollution. *Atmos. Chem. Phys.* **20**, 14917–14932 (2020).
45. van Geffen, J. et al. S5P TROPOMI NO2 slant column retrieval: method, stability, uncertainties and comparisons with OMI. *Atmos. Meas. Tech.* **13**, 1315–1335 (2020).
46. Veefkind, J. P. et al. TROPOMI on the ESA Sentinel-5 Precursor: A GMES mission for global observations of the atmospheric composition for climate, air quality and ozone layer applications. *Remote Sens. Environ.* **120**, 70–83 (2012).
47. Vigouroux, C. et al. TROPOMI–Sentinel-5 Precursor formaldehyde validation using an extensive network of ground-based Fourier-transform infrared stations. *Atmos. Meas. Tech.* **13**, 3751–3767 (2020).
48. De Smedt, I. et al. Algorithm theoretical baseline for formaldehyde retrievals from S5P TROPOMI and from the QA4ECV project. *Atmos. Meas. Tech.* **11**, 2395–2426 (2018).
49. Jin, X., Fiore, A., Boersma, K. F., Smedt, I. D. & Valin, L. Inferring changes in summertime surface ozone–NOx–VOC chemistry over U.S. urban areas from two decades of satellite and ground-based observations. *Environ. Sci. Technol.* **54**, 6518–6529 (2020).
50. Wang, W., van der A, R., Ding, J., van Weele, M. & Cheng, T. Spatial and temporal changes of the ozone sensitivity in China based on satellite and ground-based observations. *Atmos. Chem. Phys.* **21**, 7253–7269 (2021).
51. Liu, J. et al. Assessing the ratios of formaldehyde and glyoxal to NO2 as Indicators of O3–NOx–VOC sensitivity. *Environ. Sci. Technol.* **55**, 10935–10945 (2021).
52. Ji, X. et al. Ozone profiles without blind area retrieved from MAX-DOAS measurements and comprehensive validation with multi-platform observations. *Remote Sens. Environ.* **284**, 113339 (2023).


## Acknowledgements

We would like to express our gratitude to Fusheng Mou and SuWen Li of Huaibei Normal University for their assistance. We would like to thank the Ministry of Ecology and Environment of China for the O3, NO2 and CO data. We would like to thank the ERA5 data developers and TROPOMI data developers for providing free and open source materials. Financial support. This research was supported by grants from the Anhui Provincial Natural Science Foundation "Jianghuai Meteorological" Joint Fund (2208085UQ04), National Natural Science Foundation of China (U21A2027, 42207113), Anhui Meteorological Bureau Special Program for Innovation and Development (CXB202303), East China Regional Meteorological Science and Technology Collaborative Innovation Fund (QYHZ202317), and China Meteorological Administration " Application of quantum technology in meteorological detection " Youth Innovation Team Project (No.CMA2024QN11). Anhui Meteorological Service, Independent Innovation and Development Project (AHQXZC202203). Jianghuai Meteorological Joint Open Fund (2023QXTC03).

## Author contributions

C. L., C. X, and Y., C. conceived and supervised the study; Z. W. analyzed the data; Z. W. wrote the manuscript with input from C. L., C. X, and Y., C.; C. S., and H. Z. reviewed and commented on the paper; All authors contributed to discuss the results and revised manuscript.

## Competing interests

The authors declare no competing interests.

## Additional information

**Supplementary information** The online version contains supplementary material available at https://doi.org/10.1038/s41612-024-00855-3.

**Correspondence** and requests for materials should be addressed to Chengzhi Xing, Yujia Chen or Cheng Liu.

[1]Anhui Province Key Laboratory of Atmospheric Science and Satellite Remote Sensing, Anhui Institute of Meteorological Sciences, Hefei 230031, China. [2]Shouxian National Climatology Observatory, Huaihe River Basin Typical Farm Eco–meteorological Experiment Field of CMA, Shouxian 232200, China. [3]Information Materials and Intelligent Sensing Laboratory of Anhui Province, Anhui University, Hefei 230601, China. [4]School of Environmental Science and Engineering, Suzhou University of Science and Technology, Suzhou 215009, China. [5]Institute of Big Data for Vocational Education, Guangdong Polytechnic of Science and Technology, Zhuhai 519000, China. [6]Anhui Disaster Warning and Agricultural Meteorological Information Center, Hefei, Anhui 230031, China. [7]Jiangxi Ecological Meteorology Center, Nanchang 330096, China. [8]Nanchang National Climate Observatory, Nanchang 330043, China. [9]Key Lab of Environmental Optics and Technology, Anhui Institute of Optics and Fine Mechanics, Hefei Institutes of Physical Science, Chinese Academy of Sciences, Hefei 230031, China. [10]Department of Precision Machinery and Precision Instrumentation, University of Science and Technology of China, Hefei 230026, China. [11]Center for Excellence in Regional Atmospheric Environment, Institute of Urban Environment, Chinese Academy of Sciences, Xiamen 361021, China. [12]Key Laboratory of Precision Scientific Instrumentation of Anhui Higher Education Institutes, University of Science and Technology of China, Hefei 230026, China. ✉e-mail: xingcz@aiofm.ac.cn; chenyj18@mail.ustc.edu.cn; chliu81@ustc.edu.cn